nature nanotechnology

ARTICLES

https://doi.org/10.1038/s41565-022-01142-z

Check for updates

Wavelike electronic energy transfer in donor–acceptor molecular systems through quantum coherence

Fan-Fang Kong[1,5], Xiao-Jun Tian[1,5], Yang Zhang[1,2,3]✉, Yao Zhang[1,2,3], Gong Chen[1], Yun-Jie Yu[1], Shi-Hao Jing[1], Hong-Ying Gao[1,4], Yi Luo[1,2,3], Jin-Long Yang[1,2,3], Zhen-Chao Dong[1,2,3]✉ and J. G. Hou[1]✉

Quantum-coherent intermolecular energy transfer is believed to play a key role in light harvesting in photosynthesis and photovoltaics. So far, a direct, real-space demonstration of quantum coherence in donor–acceptor systems has been lacking because of the fragile quantum coherence in lossy molecular systems. Here, we precisely control the separations in well-defined donor–acceptor model systems and unveil a transition from incoherent to coherent electronic energy transfer. We monitor the fluorescence from the heterodimers with subnanometre resolution through scanning tunnelling microscopy induced luminescence. With decreasing intermolecular distance, the dipole coupling strength increases and two new emission peaks emerge: a low-intensity peak blueshifted from the donor emission, and an intense peak redshifted from the acceptor emission. Spatially resolved spectroscopic images of the redshifted emission exhibit a σ antibonding-like pattern and thus indicate a delocalized nature of the excitonic state over the whole heterodimer due to the in-phase superposition of molecular excited states. These observations suggest that the exciton can travel coherently through the whole heterodimer as a quantum-mechanical wavepacket. In our model system, the wavelike quantum-coherent transfer channel is three times more efficient than the incoherent channel.

Intermolecular electronic energy transfer (EET) in a donor–acceptor system is a ubiquitous photophysical process, important for photosynthesis and photovoltaics[1–4]. Its mechanism depends critically on the intermolecular distance and orientation[5–8]. For relatively large distances, d, of about 2–10 nm (refs. [9,10]), the excitation energy is transferred from the donor to the acceptor through dipole interactions between two independent oscillating transition dipoles, following the Förster resonance energy transfer (FRET) mechanism with a d^{-6} distance-dependent transfer rate. With a decrease in the intermolecular distance, the EET could be dominated by the Dexter mechanism that involves the overlap of electronic orbitals[6,8], with a rate following an exponential distance dependency. On the other hand, at very small intermolecular distances, intermolecular EET processes can go beyond the conventional Förster–Dexter picture[5,6]; the excited states of the donor and acceptor can be entangled with each other, resulting in the delocalization of the excitation energy and the occurrence of electronic coherence in the EET process[7,8,11]. Nevertheless, such electronic coherence is believed to be very fragile in lossy and complicated molecular systems interacting with an external thermal bath, and it was not until 2007 that researchers reported the direct evidence of such coherent energy transfer in light-harvesting systems through the quantum-beating signals in two-dimensional electronic spectroscopy[12–15]. However, subsequent studies have tended to suggest that the observed oscillation signals are correlated with vibronic coupling[16–20]. Therefore, direct experimental evidence for the existence of the EET process with electronic coherence in donor–acceptor molecular systems remains elusive.

One desirable approach for demonstrating the existence of electronic coherence is to attain a simple and well-defined donor–acceptor molecular system with controlled separations and orientations as well as energy dissipation. Furthermore, to reveal the underlying microscopic mechanism, it is also highly desirable to have optical access to each individual constituent of a donor–acceptor system to see how the energy flows. Scanning tunnelling microscopy (STM) induced luminescence (STML), a technique that combines highly localized electron excitations with optical detection[21–25], offers a unique platform for the real-space investigation of intermolecular EET processes due to its capabilities of molecular manipulation and subnanometre-resolved spectroscopic imaging beyond the far-field optics[26–30]. Elegant examples include the demonstrations of coherent dipole–dipole coupling for a homodimer[31,32] and incoherent resonant energy transfer for heterogeneous dimers[33] and trimers[34]. However, several long-standing and fundamental issues on EET[5,6,20,35] remain to be clarified experimentally. Does electronic coherence exist in a donor–acceptor heterodimer system? If yes, at what intermolecular distance and how will the coherent EET emerge? How much more efficient is the coherent EET channel than the incoherent FRET channel? To address these issues, we first construct well-defined donor–acceptor systems composed of different metal-centred phthalocyanine molecules and then examine the evolution of their STML spectra and spectroscopic images from the coupled molecular systems at various controlled intermolecular distances. We find that the incoherent-to-coherent transition in energy-transfer processes occurs when the intermolecular distance

[1]Hefei National Research Center for Physical Sciences at the Microscale and Synergetic Innovation Center of Quantum Information and Quantum Physics, University of Science and Technology of China, Hefei, China. [2]School of Physics and Department of Chemical Physics, University of Science and Technology of China, Hefei, China. [3]Hefei National Laboratory, Hefei, China. [4]School of Chemical Engineering and Technology, Tianjin University, Tianjin, China. [5]These authors contributed equally: Fan-Fang Kong, Xiao-Jun Tian. ✉e-mail: zhyangnano@ustc.edu.cn; zcdong@ustc.edu.cn; jghou@ustc.edu.cn

d is smaller than 1.72 nm. Furthermore, the quantum-coherent energy transfer is found to be dipole-orientation-dependent, which inspires us to propose a new criterion for the occurrence of quantum-coherent EET. In addition, the coherent EET channel is found to be about three times more efficient than the incoherent channel in a one-step transfer process, highlighting the advantage of coherent channels in EET processes in large molecular networks.

Incoherent energy transfer in donor–acceptor heterodimers

Figure 1a shows a schematic of the STML experiments for investigating the intermolecular EET from a donor (platinum phthalocyanine (PtPc)) to an acceptor (zinc phthalocyanine (ZnPc)), with the molecules decoupled by a three-monolayer (3ML) NaCl spacer from the Ag(100) substrate underneath to suppress metal-induced energy dissipation for molecular excitons. Selection of the phthalocyanine molecules is based on the considerations of their rich optoelectronic properties and their structural similarities to the porphyrin core of chlorophyll molecules in light-harvesting complexes. As depicted in Fig. 1b, the molecules are found to show characteristic four-lobe patterns for phthalocyanines, but with two different orientations, which are probably due to the different adsorption sites of the molecular centres (see Extended Data Fig. 1). Figure 1c shows the STML spectra obtained from the isolated single PtPc and ZnPc molecules adsorbed on a 3ML NaCl island, with a sharp emission peak at 637.7 nm (~1.945 eV) for PtPc and a less sharp peak at 652.3 nm (~1.901 eV) for ZnPc (see Supplementary Section 1). Both emission peaks arise from the intrinsic Q(0,0) transition of the neutral molecular states[31,36]. The corresponding STML images all exhibit dark-centre–bright-lobe patterns, as illustrated in the insets of Fig. 1c. Such imaging patterns are caused by the dipole symmetry of the whole system for a metal-centred phthalocyanine molecule with doubly degenerate lowest unoccupied molecular orbitals and the resultant two equivalent orthogonal transition dipoles[26,31]. We would like to note that these imaging patterns can serve as a criterion for determining the independent emission behaviour from a phthalocyanine molecule.

We then construct molecular heterodimers by pushing an isolated ZnPc[31] towards an isolated PtPc and investigate the EET through molecular fluorescence, as exemplified in Fig. 1d for a PtPc–ZnPc heterodimer with a centre-to-centre intermolecular distance (d) of ~2.21 nm. Since the optical bandgap of PtPc is larger than that of ZnPc, the PtPc molecule acts as a donor and the ZnPc molecule acts as an acceptor. Interestingly, as shown in Fig. 1d, when the tip is positioned above the PtPc molecule (namely, only the PtPc is excited by the highly localized electrons), not only is the PtPc Q(0,0) emission (P_{PtPc}) detected but also the ZnPc Q(0,0) emission ($P_{ZnPc\text{-}tr}$) can be observed. Such an observation of $P_{ZnPc\text{-}tr}$ clearly demonstrates the occurrence of EET from the excited PtPc donor to the neighbouring ZnPc acceptor. On the other hand, no discernible PtPc peak is observed when exciting on the ZnPc, which indicates a one-way energy transfer from the PtPc donor to the ZnPc acceptor. It is interesting to note that the detected ZnPc fluorescence intensity is found to depend on the excitation position of the tip above the PtPc. As shown in Fig. 1d, at an excitation voltage of −2.8 V, the $P_{ZnPc\text{-}tr}$ intensity for the tip positioned above the PtPc centre is evidently stronger than those at the PtPc lobes. Such a spatially dependent distribution of $P_{ZnPc\text{-}tr}$ intensities and the related EET feature can be further revealed through spatially resolved spectroscopic imaging over the constructed PtPc–ZnPc heterodimer, as shown in Fig. 1e–g. Such behaviour is believed to originate from the most efficient electron excitation at the PtPc centre, since the local density of the electronic states is highest there according to the differential conductance (dI/dV) mapping of a single PtPc at a voltage of −2.8 V (see Extended Data Fig. 2 and Supplementary Section 2). The dark-centre–bright-lobe patterns observed for both P_{PtPc} (Fig. 1f) and $P_{ZnPc\text{-}ex}$ (right in Fig. 1g, green colour) resemble that of an isolated single phthalocyanine molecule directly excited by tunnelling electrons, thus suggesting that the EET process occurs between two independent transition dipoles. Note that the $P_{ZnPc\text{-}tr}$ peak via the energy-transfer channel is blueshifted from the $P_{ZnPc\text{-}ex}$ peak via direct electron excitations (Fig. 1h), which is mainly caused by the tip-induced photonic Lamb shift[37,38] (see Supplementary Section 3).

To investigate the change in intermolecular EET rates at varying intermolecular distances and decipher the mechanisms, we monitor the P_{PtPc} and P_{ZnPc} intensity evolution at different separations (see Extended Data Fig. 1). As exemplified in Fig. 2a, when d is decreased, the observed P_{ZnPc} peak becomes stronger, accompanied by a decrease in the P_{PtPc} intensity. Such a tendency is better illustrated in Fig. 2b for $d \geq 1.72$ nm, which reflects the evident enhancement of the EET rate at smaller separations. We note that the observed distance-dependent tendency in this incoherent EET regime is similar to a previous report for different phthalocyanines[34].

Based on our theoretical calculations (Supplementary Section 5), the intermolecular EET processes observed here probably follow the FRET mechanism, with a d^{-6} transfer-rate dependency. Indeed, if we analyse the evolution of the ZnPc emission intensity (I_{ZnPc}) in Fig. 2b for $d \geq 1.72$ nm using $I_{ZnPc} = A/(1 + Bd^6)$ (see Supplementary Section 6), the fitting curve agrees approximately with the experimental data. Such an agreement in turn substantiates the dominant role of a FRET mechanism for this distance region, whose physical picture is schematically illustrated in Fig. 2c–e. Specifically when $d \geq 1.72$ nm, the excitation energy is transferred from the PtPc to the vibronic excited state of the ZnPc in an incoherent and one-way manner through the interaction between the two independent transition dipoles of the phthalocyanine molecules. Note that the sequential charge-transfer-assisted EET mechanism[33,34] is believed to play only a minor role here (Supplementary Section 7).

Coherent energy transfer in donor–acceptor heterodimers

When $d < 1.72$ nm, the separations between the nearest edges of the π-conjugated phthalocyanines become so close that they go beyond the van der Waals contact because of the locking effect of the underlying NaCl lattice (see Supplementary Section 8). Strikingly, in this situation, as illustrated in Fig. 2b for $d = 1.52$ nm and 1.41 nm, the P_{ZnPc} intensity drops abruptly, which suggests that the EET process has entered a new regime. As shown in Fig. 3a, for the PtPc and ZnPc molecules in a close-contact configuration ($d = 1.41$ nm), evident spectral changes are observed at six different representative sites over the heterodimer. The STML spectral profiles are different from each other in terms of the emission modes and intensities, with four emission modes highlighted in the different shaded areas. Remarkably, apart from the P_{PtPc} and P_{ZnPc} peaks, two new emission peaks show up, with a strong P_{dimer} peak at ~657.5 nm that is redshifted from the acceptor emission (P_{ZnPc}) and another very weak P'_{dimer} peak at ~636.3 nm that is blueshifted from the donor emission (P_{PtPc}). Of particular interest is the emergence of the strong and narrowed P_{dimer} peak that appears regardless of where the tip is positioned, either above PtPc or on ZnPc. Both the emergence of these new emission peaks and the associated delocalized excitonic nature indicate the occurrence of coherent dipole coupling between PtPc and ZnPc in the heterodimer[5,31,39]. In other words, in this regime, the excitation energy can transfer in a two-way manner (that is, not only from the donor to acceptor but also from the acceptor back to the donor), which is different from the incoherent one-way FRET process.

Spectroscopic imaging over the heterodimer provides a panoramic view of the spatial localization or delocalization feature for different molecular excitonic modes (Fig. 3c–e). Remarkably, as shown in Fig. 3b,c, the imaging pattern of the P_{dimer} mode spreads over both the PtPc and ZnPc molecules and resembles a 'σ antibonding'-like pattern along the dimer axial direction. Such a pattern, together with the redshifting of the peak (Fig. 3a), is a clear indication

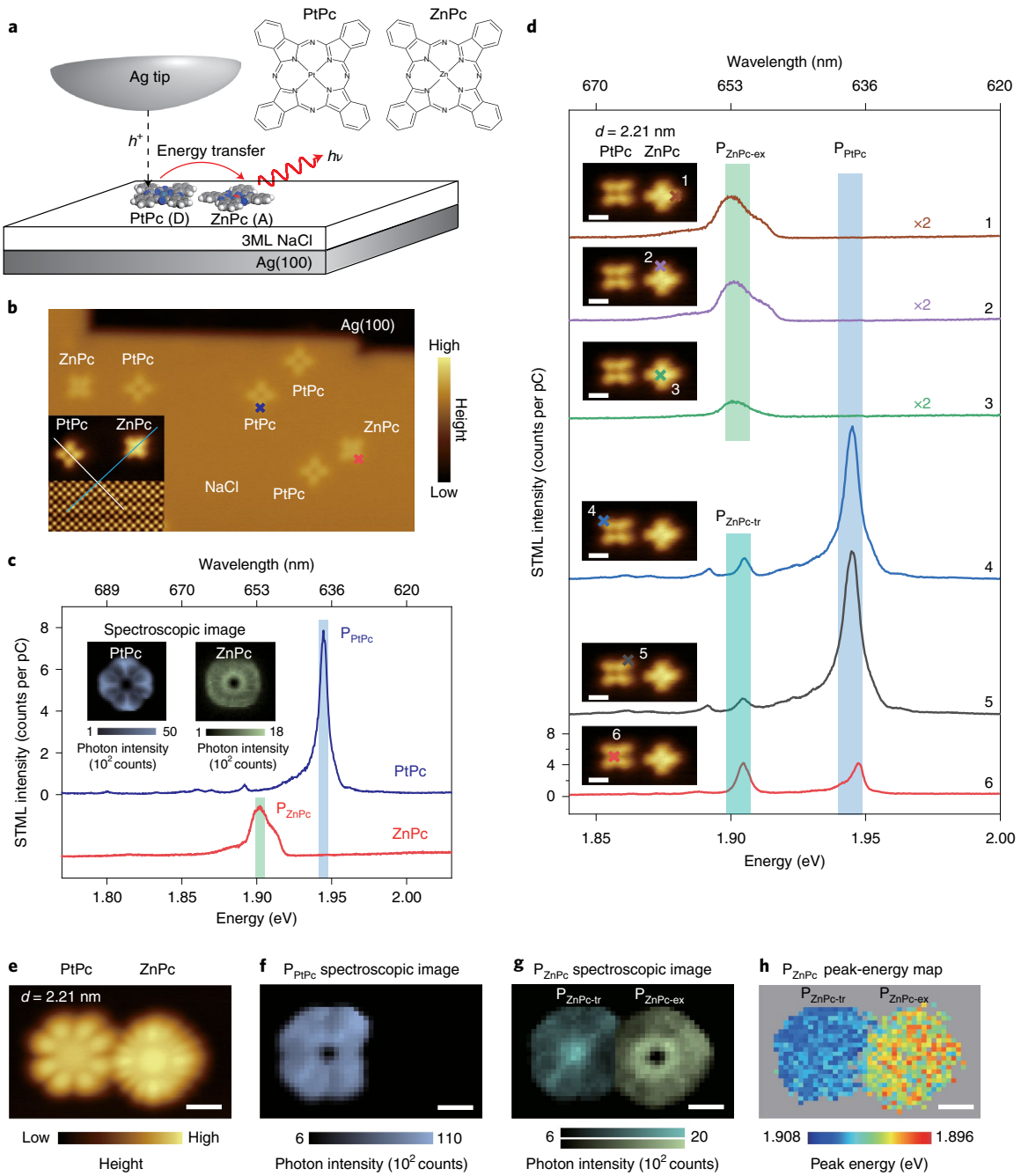

Fig. 1 | Intermolecular energy transfer in a constructed PtPc–ZnPc dimer at a relatively large distance of ~2.21 nm. a, Schematic of the STML experiments on intermolecular EET between the donor (D; PtPc) and acceptor (A; ZnPc) molecules on 3ML NaCl/Ag(100). The corresponding molecular structures are shown on the top right. **b**, STM image of single PtPc and ZnPc molecules adsorbed on 3ML NaCl/Ag(100) (−2.1 V, 2 pA; 22 × 13 nm). Inset: to identify the molecular adsorption sites, the STM image is acquired under different scanning conditions (7 × 7 nm), where the upper part is acquired at −2.1 V and 2 pA to highlight the molecular skeleton, and the lower part is acquired at 0.1 V and 500 pA to resolve the chlorine ions. The molecular adsorption configurations are detailed in Extended Data Fig. 1. **c**, STML spectra acquired from the isolated single PtPc and ZnPc molecules marked, respectively, with blue and red crosses in **b**. Conditions: −2.8 V and 30 pA with an integration time of 30 s. Inset: the STML spectroscopic images of the Q(0,0) emission from a single PtPc molecule (−2.8 V, 30 pA, 1 s per pixel; 4 × 4 nm, 40 × 40 pixels; integrated over the blue shaded region: 1.942–1.948 eV); and a single ZnPc molecule (−2.8 V, 100 pA, 1 s per pixel; 4 × 4 nm, 40 × 40 pixels; integrated over the green shaded region: 1.899–1.905 eV). See Supplementary Section 1 for the lineshape analysis. **d**, Site-dependent STML spectra (−2.8 V, 30 pA, 30 s) acquired over a constructed PtPc–ZnPc heterodimer at the positions marked in the respective inset STM image (−2.1 V, 2 pA). All STML spectra are offset for clarity. **e**–**g**, STM topograph (−2.8 V, 2 pA) (**e**) and STML spectroscopic images (**f**,**g**) of a constructed PtPc–ZnPc heterodimer with $d = 2.21$ nm. Spectroscopic images (−2.8 V, 30 pA, 1 s per pixel) are obtained through integration over the different emission peaks highlighted with different shaded regions in **d** (PtPc, 1.940–1.949 eV; ZnPc, 1.898–1.907 eV). Different colours are used to distinguish the different excitation origin of the ZnPc emission: cyan denotes the ZnPc Q(0,0) emission obtained directly through tunnelling electron excitation ($P_{ZnPc\text{-}ex}$); green denotes the ZnPc Q(0,0) emission excited through the EET process from the neighbouring PtPc ($P_{ZnPc\text{-}tr}$). **h**, Spatial distribution of ZnPc Q(0,0) peak energies obtained from the experimental spectroscopic image, which was acquired for the same area in **e**. Scale bars in **d**–**h**, 1 nm.

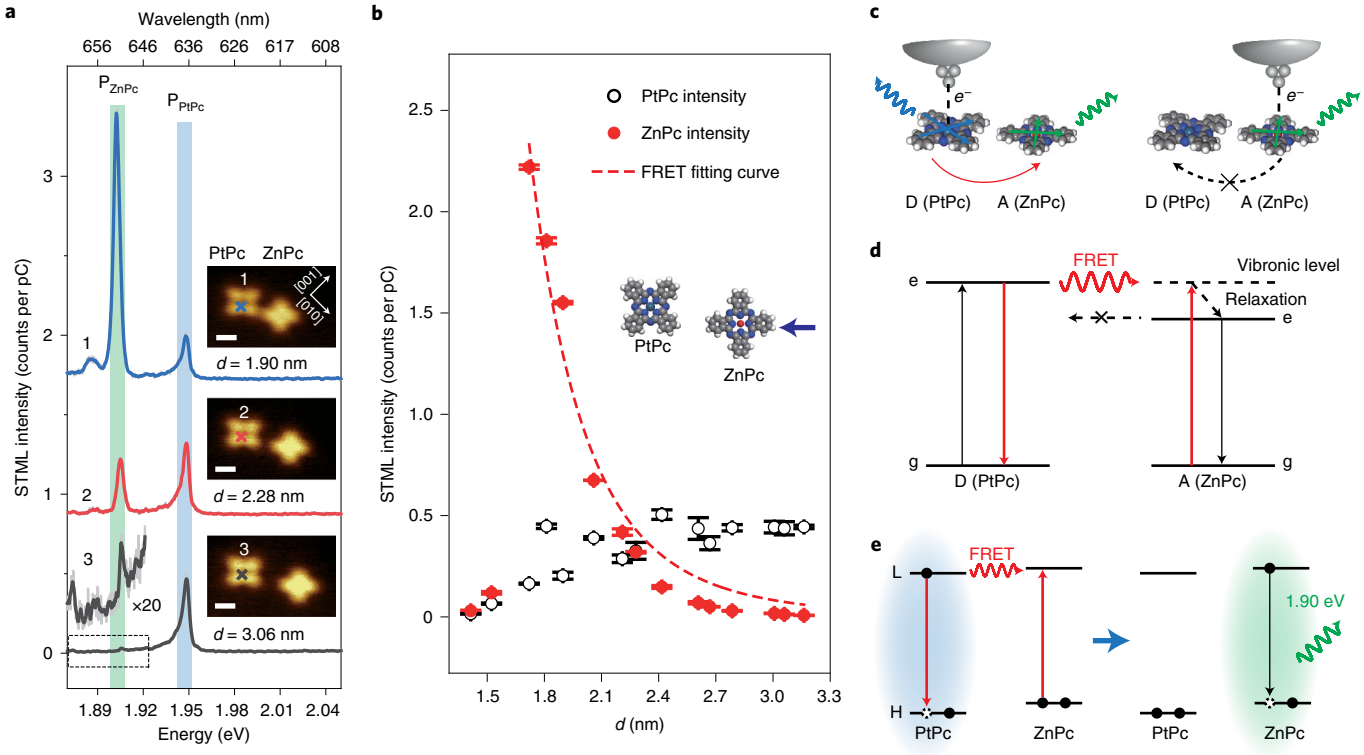

Fig. 2 | Hopping-like FRET at relatively large distances ($d \geq 1.72$ nm). a, STML spectral evolution with decreasing intermolecular distance, as exemplified for heterodimers with $d = 3.06$ nm, 2.28 nm and 1.90 nm. STML spectra were acquired from the PtPc molecular centre (−2.8 V, 30 pA, 30 s). The inset STM images show the heterodimers for $d = 3.06$ nm, 2.28 nm and 1.90 nm, respectively, with arrows marking the orientations of the NaCl lattice. Conditions for the inset STM images: −2.1 V, 2 pA. The dashed rectangle on the bottom left marks the range of the black STML spectrum that is amplified by 20 times. The shaded bands labelled as P_{PtPc} and P_{ZnPc} indicate the corresponding peak positions. All STML spectra are offset for clarity. Scale bars, 1 nm. **b**, STML intensities in terms of the peak heights of the Q(0,0) emissions for PtPc (open black circles) and ZnPc (filled red circles) at different intermolecular distances d (from 3.16 nm to 1.41 nm) when the tip is positioned above the PtPc centre. Each peak-height value is averaged over five datasets with error bars representing standard deviations. To avoid complications caused by site-dependent excitation issues, the STML spectra acquired at the PtPc centre are used to evaluate the EET rates. The red dashed line is a fitting curve that uses a function of $I_{ZnPc} = A/(1 + Bd^6)$, where A and B are fitting parameters. In our experiments, the occurrence of intermolecular energy transfer can be detected for a distance of up to $d = 3.41$ nm if a long integration time is used (detailed in Supplementary Section 4). The inset shows the schematic of a PtPc–ZnPc heterodimer, with the blue arrow indicating the manipulation direction of ZnPc. **c**, Schematics illustrating the one-way energy-transfer process from PtPc to ZnPc. **d**,**e**, Schematics of the resonance energy transfer between the PtPc and ZnPc molecules for $d \geq 1.72$ nm. The energy-level alignments were drawn by referring to the measured fluorescence energies (**d**) and dI/dV curves (**e**) (see Extended Data Fig. 2 and Supplementary Section 7). g, ground state; e, excited state; L, lowest unoccupied molecular orbital; H, highest occupied molecular orbital.

of the occurrence of a delocalized excitonic mode due to coherent in-line in-phase dipole coupling along the axial direction[31,32], as illustrated in Fig. 3f for the P_{dimer} mode. Such in-phase dipole coupling is associated with the symmetric quantum superposition of the products of states of both the PtPc and ZnPc molecules, with only one molecule in the excited state and the other in the ground state[31,32,39] (see Supplementary Section 10). In addition, the assignment of the in-line in-phase dipole coupling configuration for the P_{dimer} is substantiated further by the theoretical simulations of both spectroscopic images and tip-induced photonic Lamb shifts[38] (see Extended Data Figs. 3 and 4 as well as Supplementary Section 11).

The emergence of the two new excitonic modes (that is, P_{dimer} and P'_{dimer}) suggests that the dipole coupling strength has reached an extent to beat the system dissipation so that the donor and acceptor can be coherently coupled. Such a strong dipole coupling leads to a fast energy oscillation frequency that enables the excitation energy to oscillate back and forth between the PtPc and ZnPc components before dissipation[5,8]. The simultaneous detection for the emission of both 'bright' (in-line in-phase P_{dimer}) and 'dark' (in-line out-of-phase P'_{dimer}) modes enables the excitonic splitting (or coupling strength) to be obtained directly. As detailed in Supplementary Section 10.1, the in-line dipole coupling strength ($|V|$) is estimated to be ~23 meV. Such a coupling strength leads to a fast energy oscillation frequency (Ω) of about $9.4 \times 10^{13}\,s^{-1}$ between the PtPc and ZnPc sites, estimated via $\Omega = 2\sqrt{\Delta^2 + V^2}/\hbar$ (ref. [5]), where Δ is half of the optical bandgap difference between PtPc and ZnPc, and $\hbar$ is the reduced Planck constant. The oscillation frequency is faster than molecular vibrational relaxations (~$10^{12}\,s^{-1}$)[40] and, more importantly, it is also faster than the energy dissipation over either the PtPc site ($\Gamma_a \approx 1.1 \times 10^{13}\,s^{-1}$) or the ZnPc site ($\Gamma_b \approx 1.7 \times 10^{13}\,s^{-1}$), with the dissipation approximated by the total decay rate of the molecular excited states. Thus, the excitation energy can transfer coherently in coupled donor–acceptor systems as a spatially confined quantum-mechanical wavepacket, with fixed phase relationships between the wavefunctions of excited states for different phthalocyanines[7]. In this sense, the coherent EET here can be pictorially described as wavelike EET. Notably, the quantum-coherent EET in the PtPc–ZnPc heterodimer is an electronic coherence, since the P_{dimer} and P'_{dimer} modes shift around the electronic origin (that is, Q(0,0)) of either ZnPc or PtPc (Fig. 3f)[41]. We note that the quantum coherence will not be destroyed by the approaching tip for a stable tunnelling regime of up to 4.0 nA (Supplementary Section 12).

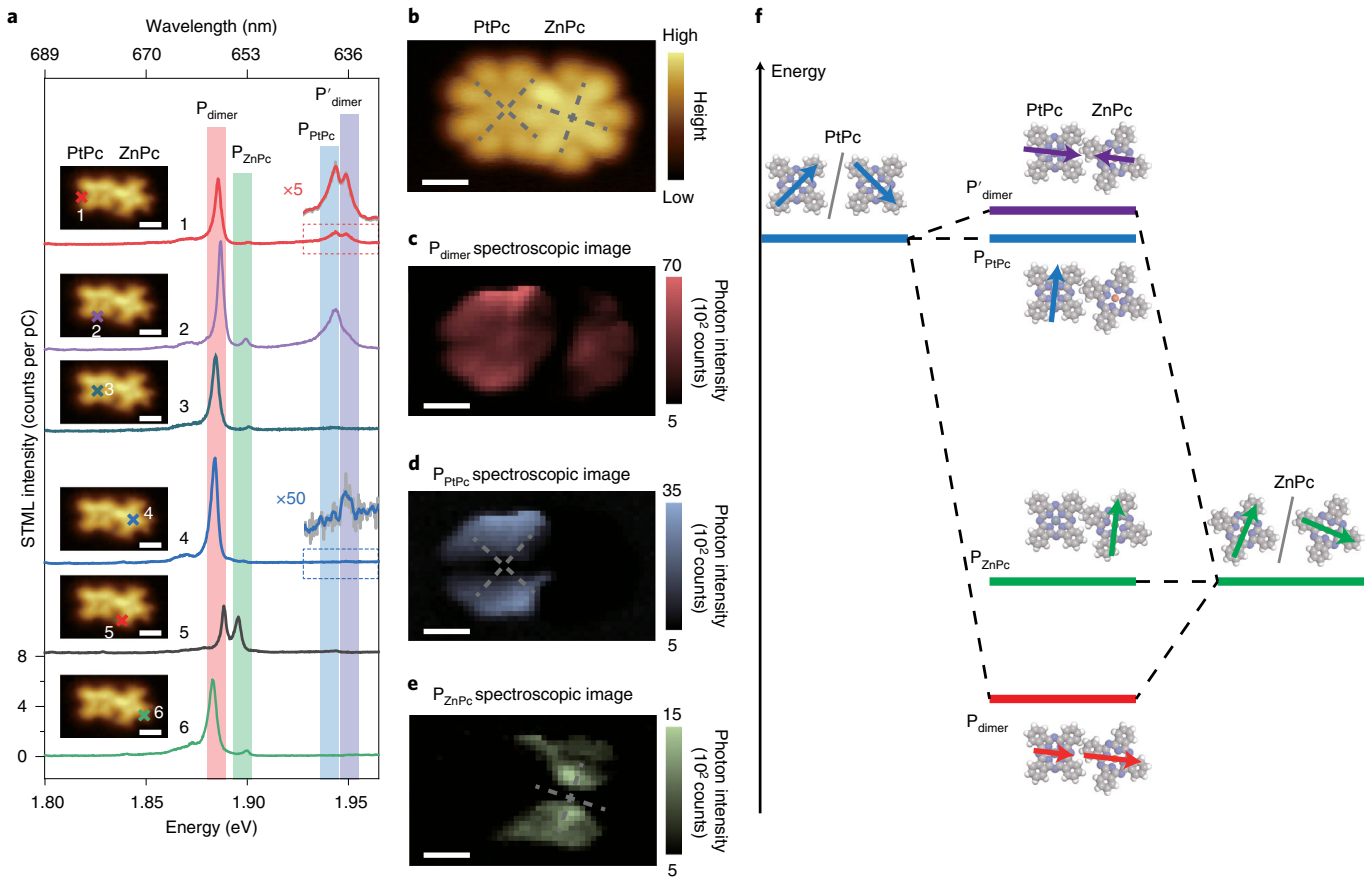

Fig. 3 | Dipole-orientation-dependent quantum-coherent energy transfer in a constructed PtPc–ZnPc heterodimer in close contact (d = 1.41 nm). **a**, Site-dependent STML spectra (−2.8 V, 30 pA, 30 s) acquired at six representative sites over the heterodimer, as marked with crosses in the inset STM images (−2.1 V, 2 pA). The red (blue) dashed rectangle marks the range of the red (blue) STML spectrum that is amplified by 5 (50) times. All STML spectra are offset for clarity. The peak at ~638.5 nm is assigned to P_{PtPc}, and the peak at ~654.0 nm to P_{ZnPc}. Both are redshifted slightly from those in Fig. 1, probably due to the energy difference of the van der Waals interactions between the excited and ground states of the closely contacted molecules. Scale bars, 1 nm. **b**–**e**, STM topograph (−2.8 V, 2 pA) (**b**) and STML spectroscopic images (**c**–**e**) of a constructed heterodimer with d = 1.41 nm. The STML spectroscopic images for the emission peaks P_{dimer} (**c**), P_{PtPc} (**d**) and P_{ZnPc} (**e**) are obtained by integrating over the ranges indicated by the respective shaded bands in **a** (−2.8 V, 30 pA, 1 s per pixel) (P_{dimer}, 1.881–1.890 eV; P_{PtPc}, 1.938–1.947 eV; P_{ZnPc}, 1.893–1.902 eV). In **b**,**d**,**e**, the skeletons of some phthalocyanine molecules are indicated by grey crosses as a guide to the eye. Note that the P_{dimer} emission peak is intrinsically different from a nearby vibronic peak of PtPc, as detailed in Supplementary Section 9. Scale bars, 1 nm. **f**, Exciton interaction diagram for the coherently coupled and uncoupled emission modes of the heterodimer. The corresponding dipole arrangements of the molecules are also plotted.

In the coherent EET regime, there are two types of coherence in EET processes[42]. One is steady-state electronic coherence, that is, quantum coherence that is associated with a superposition of excitations at different molecular sites[43], arising from a stationary perturbation of the dipole coupling. This type of coherence can be directly revealed by the steady-state STML measurements, as demonstrated here, where both the appearance of splitting-induced new peaks and associated extended σ antibonding-like imaging patterns over the donor–acceptor system suggest the formation of delocalized excitonic eigenstates. Such delocalized excitonic states are a prerequisite for the occurrence of quantum dynamics in coherent EET. The other type is the coherent superposition of excitonic eigenstates leading to periodic phase oscillation in the total wavefunction[42], usually detected via ultrafast techniques[12–14,43]. Such a coherence can be described by the off-diagonal elements in the density matrix in the basis of system eigenstates[44]. As detailed in Supplementary Section 10.3, using the Lindblad quantum master equation[45] within the framework of exciton theory[5,39,42], we can deduce oscillatory behaviour in the off-diagonal elements for the heterodimer at d = 1.41 nm with a coherence time that lasts for ~73 fs, which is long enough to complete one cycle of phase oscillation (~67 fs) before dissipation. In addition, we find that the quantum coherence associated with the phase oscillation can last longer for the heterodimer on a thicker NaCl spacer (that is, four layers, or 4ML NaCl), due to reduced energy dissipation of the molecule to the substrate (see more details in Supplementary Section 10.3).

On the other hand, unlike the coherent coupling behaviour observed for dipoles perpendicular to the axial direction in a homodimer[31], the spatial distribution of the P_{PtPc} (P_{ZnPc}) mode is mainly confined within the PtPc (ZnPc) molecule itself and is oriented perpendicular to the dimer axial direction, as shown in Fig. 3d (Fig. 3e). Such a spatial confinement suggests the localized nature of the modes along that direction, which also implies that the associated transition dipole is perpendicular to the axial direction and its dipole oscillation is independent of its neighbouring dipoles, as illustrated in Fig. 3f for the P_{PtPc} and P_{ZnPc} modes.

The understanding of the dipole-orientation-dependent behaviour of quantum-coherent EET in the donor–acceptor system is believed to associate with the dipole coupling strength and energy dissipation as well as the energy difference between PtPc and ZnPc. The lack of coherence in the EET process for the dipoles perpendicular to the axial direction inspires us to propose a new criterion for

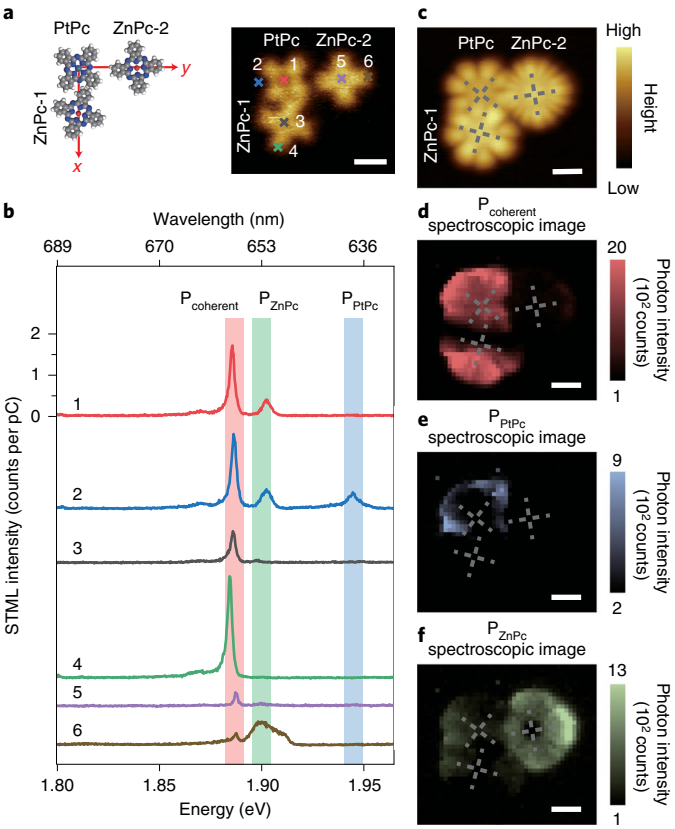

Fig. 4 | Comparison of EET efficiencies between coherent and incoherent channels through constructing molecular networks. a, Schematic (left) and STM image (right, −2.1 V, 2 pA) of a ZnPc–PtPc–ZnPc trimer structure with a right-angled shape. Scale bar, 1 nm. **b**, Site-dependent STML spectra (−2.8 V, 30 pA, 20 s) acquired at the representative sites over the trimer, as marked by the coloured crosses in **a**. All STML spectra are offset for clarity. **c**–**f**, STM topograph (−2.8 V, 2 pA) (**c**) and spectroscopic images (**d**–**f**) of the constructed trimer. The spectroscopic images for the emission peaks $P_{coherent}$ (**d**), P_{PtPc} (**e**) and P_{ZnPc} (**f**) are obtained by integrating over the ranges indicated by the respective shaded bands in **b** (−2.8 V, 30 pA, 2 s per pixel; $P_{coherent}$, 1.882–1.891 eV; P_{PtPc}, 1.940–1.949 eV; P_{ZnPc}, 1.895–1.904 eV). The skeletons of phthalocyanine molecules are indicated by grey crosses as a guide for the eye. Scale bars, 1 nm.

the occurrence of quantum-coherent EET, since the conventional criterion for the strong coupling[46,47] (that is, $\Omega > \max(\Gamma_a,\Gamma_b)$) fails to explain the observed phenomena.

To judge whether quantum-coherent EET in a heterodimer can occur or not, we need to consider the net oscillation frequency induced by the dipole coupling (Ω_{ind}^{net}), rather than the pristine oscillation frequency (Ω), as defined below (also detailed in Supplementary Section 10.4):

$$\Omega_{ind}^{net} = 2\left(\sqrt{\Delta^2+V^2} - \Delta\right)/\hbar.$$

In this case, quantum-coherent EET is found to occur when the net oscillation frequency becomes larger than the dissipation at either the PtPc (Γ_a) or ZnPc (Γ_b) site, as rationalized by the criterion proposed below:

$$\Omega_{ind}^{net} > \max\left(\Gamma_a, \Gamma_b\right).$$

As detailed in Supplementary Section 10.4, the absence of quantum-coherent EET for the dipoles perpendicular to the axial direction is due to their smaller coupling strength, leading to a net hypothetical oscillation frequency that is slower than the dissipation. Therefore, the energy transferred from the perpendicular transition dipole component of PtPc to that of ZnPc will dissipate at the ZnPc site, failing to oscillate back to PtPc.

Notably, the P_{ZnPc} peak is found to be very weak when exciting on PtPc (curves 1–3 in Fig. 3a), in sharp contrast to the strong P_{dimer} peak. Such an observation suggests that the wavelike quantum-coherent EET channel is more efficient than the hopping-like incoherent EET channel in the heterodimer, as exemplified by a small peak-height ratio for P_{ZnPc}/P_{dimer} of about 8% (curve 2 in Fig. 3a).

Energy transfer in molecular architectures beyond dimers

In molecular networks, the quantitative evaluation of how much more efficient the coherent EET channel is than the incoherent channel is important but challenging due to the difficulty of tuning the coherence on and off experimentally[35]. To this end, we design a right-angled 'trimer' structure with different intermolecular distances for tuning the energy-transfer channels, as shown in Fig. 4a. The intermolecular distance is 1.41 nm along the x direction and 1.81 nm along the y direction, which is expected to yield a coherent channel along the x direction and an incoherent channel along the y direction according to the observations and analyses for the heterodimers shown in Figs. 2 and 3. Indeed, as illustrated by the site-dependent STML spectra in Fig. 4b and the spectroscopic images in Fig. 4d–f, the excitation energy on PtPc is transferred both coherently to the adjacent ZnPc-1 (as evidenced by the $P_{coherent}$ mode, which is associated with the in-line in-phase dipole coupling between PtPc and ZnPc-1) and incoherently to ZnPc-2 (as evidenced by the P_{ZnPc} mode). As detailed in Supplementary Section 13, for the molecular architecture demonstrated here we find that the coherent EET channel is about three times as efficient as the incoherent channel in a one-step transfer process.

Furthermore, we would like to emphasize that, if the molecules can be properly arranged in a molecular network, such as in the linear trimer shown in Fig. 5a with the central PtPc tightly bridging two ZnPc molecules, the excitation energy can delocalize over the whole network instantaneously, as revealed by the further red-shifted emission peak (P_{trimer}) in Fig. 5b and the associated further extended σ antibonding-like pattern of the spectroscopic image in Fig. 5c (detailed in Supplementary Section 14). Considering the hopping-like and step-wise nature of the incoherent energy transfer, the wavelike coherent EET is thus believed to be much more efficient than the incoherent FRET process in large molecular networks.

Conclusions

We have visualized in real space the incoherent-to-coherent transition in intermolecular EET processes between a donor (PtPc) and an acceptor (ZnPc) as the intermolecular distance is successively decreased. For $d \geq 1.72$ nm, the EET process follows the FRET mechanism in a one-way, hopping-like and incoherent manner with a d^{-6} rate dependency. Strikingly, below this distance (for example, 1.41 nm), two new emission peaks (P_{dimer} and P'_{dimer}) emerge due to the strong in-line dipole coupling, with the P_{dimer} emission appearing all over the heterodimer and exhibiting a σ antibonding-like imaging pattern, which suggests transfer in a two-way manner. The associated energy oscillation frequency between the donor and acceptor sites is found to be faster than the energy dissipation at either site. Such a fast oscillation frequency, together with the delocalized nature of the excitonic state, clearly suggests the occurrence of wavelike quantum-coherent EET. Notably, such quantum-coherent EET does not exist for the transition dipoles perpendicular to the axial direction, which inspired us to come up with a new criterion based on the dipole-coupling-induced net oscillation frequency regarding the occurrence of quantum-coherent EET. Furthermore, the

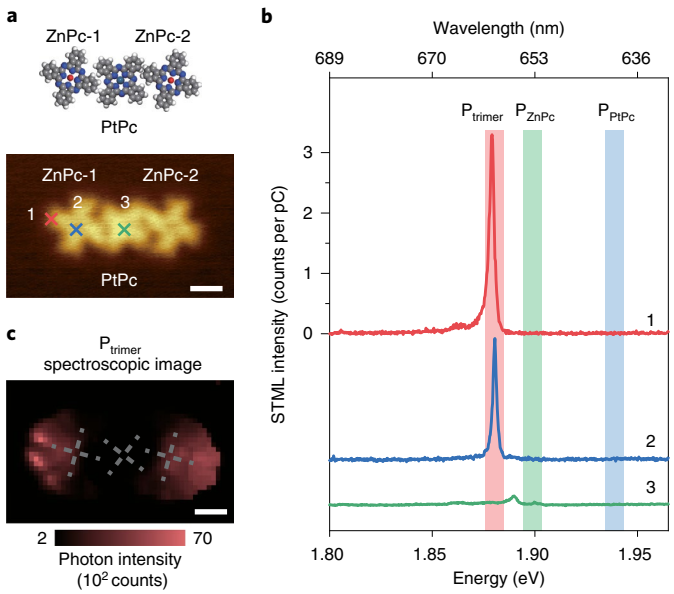

Fig. 5 | Quantum-coherent energy transfer in a linear trimer. a, Top: schematic ZnPc–PtPc–ZnPc trimer structure. Bottom: STM image of an artificially constructed linear trimer acquired at −2.1 V and 2 pA to reveal the molecular skeletons. Scale bar, 1 nm. **b**, Site-dependent STML spectra (−2.8 V, 30 pA, 10 s) acquired at three representative sites over the trimer, as marked by the coloured crosses in **a**. All STML spectra are offset for clarity. **c**, Spectroscopic image for the P_{trimer} mode (−2.8 V, 30 pA, 3 s per pixel; P_{trimer}, 1.876–1.885 eV). The skeletons of phthalocyanine molecules are indicated by grey crosses as a guide the the eye. Scale bar, 1 nm.

coherent EET channel is found to be about three times more efficient than the incoherent channel in a one-step transfer process. Our findings provide spectral and spatial evidence for quantum-coherent EET in donor–acceptor systems at the single-molecule level. Further studies combined with ultrafast time-resolved spectroscopy will help to gain further insight into the energy-transfer dynamics, providing comprehensive guidance for the rational design of artificial molecular systems that exploit coherence to achieve optimal EET efficiencies in photosynthesis, molecular optoelectronics and quantum biology.

Online content

Any methods, additional references, Nature Research reporting summaries, source data, extended data, supplementary information, acknowledgements, peer review information; details of author contributions and competing interests; and statements of data and code availability are available at https://doi.org/10.1038/s41565-022-01142-z.

Received: 2 April 2021; Accepted: 25 April 2022;
Published online: 6 June 2022

References

1. Scholes, G. D., Fleming, G. R., Olaya-Castro, A. & van Grondelle, R. Lessons from nature about solar light harvesting. *Nat. Chem.* **3**, 763–774 (2011).
2. Romero, E., Novoderezhkin, V. I. & van Grondelle, R. Quantum design of photosynthesis for bio-inspired solar-energy conversion. *Nature* **543**, 355–365 (2017).
3. Hedley, G. J., Ruseckas, A. & Samuel, I. D. Light harvesting for organic photovoltaics. *Chem. Rev.* **117**, 796–837 (2017).
4. Dorfman, K. E., Voronine, D. V., Mukamel, S. & Scully, M. O. Photosynthetic reaction center as a quantum heat engine. *Proc. Natl. Acad. Sci. USA* **110**, 2746–2751 (2013).
5. Förster, T. in *Modern Quantum Chemistry* (ed. Sinanoglu, O.) 93–137 (Academic, 1965).
6. Olaya-Castro, A. & Scholes, G. D. Energy transfer from Förster–Dexter theory to quantum coherent light-harvesting. *Int. Rev. Phys. Chem.* **30**, 49–77 (2011).
7. May, V. & Kühn, O. *Charge and Energy Transfer Dynamics in Molecular Systems* (Wiley, 2011).
8. Govorov, A., Martínez, P. L. H. & Demir, H. V. *Understanding and Modeling Förster-type Resonance Energy Transfer (FRET): Introduction to FRET, Vol. 1* (Springer, 2016).
9. Yun, C. S. et al. Nanometal surface energy transfer in optical rulers, breaking the FRET barrier. *J. Am. Chem. Soc.* **127**, 3115–3119 (2005).
10. Deng, R., Wang, J., Chen, R., Huang, W. & Liu, X. Enabling Förster resonance energy transfer from large nanocrystals through energy migration. *J. Am. Chem. Soc.* **138**, 15972–15979 (2016).
11. Diehl, F. P. et al. Emergence of coherence through variation of intermolecular distances in a series of molecular dimers. *J. Phys. Chem. Lett.* **5**, 262–269 (2014).
12. Engel, G. S. et al. Evidence for wavelike energy transfer through quantum coherence in photosynthetic systems. *Nature* **446**, 782–786 (2007).
13. Collini, E. et al. Coherently wired light-harvesting in photosynthetic marine algae at ambient temperature. *Nature* **463**, 644–647 (2010).
14. Hayes, D., Griffin, G. B. & Engel, G. S. Engineering coherence among excited states in synthetic heterodimer systems. *Science* **340**, 1431–1434 (2013).
15. Hildner, R., Brinks, D., Nieder, J. B., Cogdell, R. J. & van Hulst, N. F. Quantum coherent energy transfer over varying pathways in single light-harvesting complexes. *Science* **340**, 1448–1451 (2013).
16. Tiwari, V., Peters, W. K. & Jonas, D. M. Electronic resonance with anticorrelated pigment vibrations drives photosynthetic energy transfer outside the adiabatic framework. *Proc. Natl. Acad. Sci. USA* **110**, 1203–1208 (2013).
17. Duan, H. G. et al. Nature does not rely on long-lived electronic quantum coherence for photosynthetic energy transfer. *Proc. Natl. Acad. Sci. USA* **114**, 8493–8498 (2017).
18. Thyrhaug, E. et al. Identification and characterization of diverse coherences in the Fenna-Matthews-Olson complex. *Nat. Chem.* **10**, 780–786 (2018).
19. Ball, P. Is photosynthesis quantum-ish? *Phys. World* **31**, 44–48 (2018).
20. Jumper, C. C., Rafiq, S., Wang, S. & Scholes, G. D. From coherent to vibronic light harvesting in photosynthesis. *Curr. Opin. Chem. Biol.* **47**, 39–46 (2018).
21. Gimzewski, J. K., Reihl, B., Coombs, J. H. & Schlittler, R. R. Photon emission with the scanning tunneling microscope. *Z. Phys. B* **72**, 497–501 (1988).
22. Berndt, R., Gimzewski, J. K. & Johansson, P. Inelastic tunneling excitation of tip-induced plasmon modes on noble-metal surfaces. *Phys. Rev. Lett.* **67**, 3796–3799 (1991).
23. Qiu, X. H., Nazin, G. V. & Ho, W. Vibrationally resolved fluorescence excited with submolecular precision. *Science* **299**, 542–546 (2003).
24. Dong, Z. C. et al. Vibrationally resolved fluorescence from organic molecules near metal surfaces in a scanning tunneling microscope. *Phys. Rev. Lett.* **92**, 086801 (2004).
25. Cavar, E. et al. Fluorescence and phosphorescence from individual molecules excited by local electron tunneling. *Phys. Rev. Lett.* **95**, 196102 (2005).
26. Chen, C., Chu, P., Bobisch, C. A., Mills, D. L. & Ho, W. Viewing the interior of a single molecule: vibronically resolved photon imaging at submolecular resolution. *Phys. Rev. Lett.* **105**, 217402 (2010).
27. Doppagne, B. et al. Electrofluorochromism at the single-molecule level. *Science* **361**, 251–255 (2018).
28. Kimura, K. et al. Selective triplet exciton formation in a single molecule. *Nature* **570**, 210–213 (2019).
29. Doppagne, B. et al. Single-molecule tautomerization tracking through space- and time-resolved fluorescence spectroscopy. *Nat. Nanotechnol.* **15**, 207–211 (2020).
30. Kuhnke, K., Große, C., Merino, P. & Kern, K. Atomic-scale imaging and spectroscopy of electroluminescence at molecular interfaces. *Chem. Rev.* **117**, 5174–5222 (2017).
31. Zhang, Y. et al. Visualizing coherent intermolecular dipole–dipole coupling in real space. *Nature* **531**, 623–627 (2016).
32. Luo, Y. et al. Electrically driven single-photon superradiance from molecular chains in a plasmonic nanocavity. *Phys. Rev. Lett.* **122**, 233901 (2019).
33. Imada, H. et al. Real-space investigation of energy transfer in heterogeneous molecular dimers. *Nature* **538**, 364–367 (2016).
34. Cao, S. et al. Energy funnelling within multichromophore architectures monitored with subnanometre resolution. *Nat. Chem.* **13**, 766–770 (2021).
35. Tomasi, S., Baghbanzadeh, S., Rahimi-Keshari, S. & Kassal, I. Coherent and controllable enhancement of light-harvesting efficiency. *Phys. Rev. A* **100**, 043411 (2019).
36. Farrukh, A. et al. Bias-polarity dependent electroluminescence from a single platinum phthalocyanine molecule. *Chin. J. Chem. Phys.* **34**, 87–94 (2020).
37. Zhang, Y. et al. Sub-nanometre control of the coherent interaction between a single molecule and a plasmonic nanocavity. *Nat. Commun.* **8**, 15225 (2017).
38. Yang, B. et al. Sub-nanometre resolution in single-molecule photoluminescence imaging. *Nat. Photonics* **14**, 693–699 (2020).

39. Kasha, M., Rawls, H. R. & Ashraf El-Bayoumi, M. The exciton model in molecular spectroscopy. *Pure Appl. Chem.* **11**, 371–392 (1965).
40. Turro, N. J. *Modern Molecular Photochemistry* (Benjamin/Cummings, 1978).
41. Womick, J. M. & Moran, A. M. Vibronic enhancement of exciton sizes and energy transport in photosynthetic complexes. *J. Phys. Chem. B* **115**, 1347–1356 (2011).
42. Lanzani, G. *The Photophysics behind Photovoltaics and Photonics* (Wiley, 2012).
43. Chenu, A. & Scholes, G. D. Coherence in energy transfer and photosynthesis. *Annu. Rev. Phys. Chem.* **66**, 69–96 (2015).
44. Cao, J. et al. Quantum biology revisited. *Sci. Adv.* **6**, eaaz4888 (2020).
45. Mohseni, M., Rebentrost, P., Lloyd, S. & Aspuru-Guzik, A. Environment-assisted quantum walks in photosynthetic energy transfer. *J. Chem. Phys.* **129**, 174106 (2008).
46. Torma, P. & Barnes, W. L. Strong coupling between surface plasmon polaritons and emitters: a review. *Rep. Prog. Phys.* **78**, 013901 (2015).
47. Chikkaraddy, R. et al. Single-molecule strong coupling at room temperature in plasmonic nanocavities. *Nature* **535**, 127–130 (2016).

Methods

All STM imaging and STML measurements were performed using a custom low-temperature ultrahigh-vacuum STM (Unisoku) combined with optical detection systems at about 7 K under a base pressure of about 1×10^{-10} torr. The Ag(100) substrate was cleaned through cycles of argon-ion sputtering and annealing. Electrochemically etched silver (Ag) tips were used, which were cleaned via electron bombardment and argon-ion sputtering, followed by tip indentations to achieve the desired nanocavity plasmon emission modes[48]. We partially covered a Ag(100) single-crystal surface with three layers of NaCl (that is, 3ML NaCl/Ag(100)) through thermal evaporation of NaCl at ~775 K. We then thermally evaporated ZnPc and PtPc molecules onto the 3ML NaCl/Ag(100) surface with the substrate kept at ~7 K. The PtPc–ZnPc dimers with different configurations were constructed via pushing a single ZnPc molecule towards a single PtPc molecule, which is achieved by approaching the STM tip to the edge of a ZnPc molecule[31,32]. Differential conductance (dI/dV) measurements were performed using a lock-in technique with a bias modulation of 10 mV (root mean square) at 329 Hz.

STM imaging and optical spectral measurements were performed in constant-current mode with the sample biased. Photons emitted from the STM junction were collected via two symmetrical double-lens channels to increase the collection efficiency. Both collection channels are connected to a liquid-nitrogen-cooled CCD (charge-coupled device) spectrometer (Princeton Instruments) for STML spectral measurements[31,49,50]. All spectra presented in this paper are not corrected for the wavelength-dependent sensitivity of photon detection systems. Spatially and spectrally resolved photon images were obtained by recording a spectrum at each pixel and assigning to each pixel the integrated emission intensities over a certain wavelength range. To remove the influence of thermal drift during the long acquisition time, for precise correlation of the emission feature with the molecular structure, we corrected the image distortions using the following procedure[31]: when acquiring an energy-resolved spectroscopic image, a reference STM image with molecular features was acquired simultaneously; the reference STM image was then deformed to make the molecular features match with an almost drift-free STM image for the same area that was acquired at a normal scanning speed; finally, the same deformation process was applied to the corresponding photon image.

The distances between the PtPc and ZnPc molecules in the present work refer to the centre-to-centre intermolecular distances (d) and have an uncertainty in a range from ±0.04 nm to ±0.08 nm. These distances are estimated based on the molecular configurations under study (see Extended Data Fig. 1) and the separation between the two nearest chlorine ions. For 3ML NaCl on Ag(100), the measured distance between the two nearest chlorine ions on the NaCl surface is 0.40 ± 0.01 nm, which is very close to the value reported in the literature[51]. The distance here is calculated by averaging over those distances from ten different datasets, each of which is obtained through a line-profile analysis across eleven chlorine ions along either the [011] or [01$\bar{1}$] direction.

We note that the difference in the tip sharpness for different tips may affect the image resolution, but the dominant feature remains essentially the same and the spectra presented in each figure were acquired using essentially the same tip. In Fig. 1h, to better extract the spatial distribution of the peak energy over the heterodimer, the nanocavity plasmon spectral backgrounds in each STML spectrum were subtracted.

Data availability

Source data are provided with this paper. All other data that support the findings of this study are available from the corresponding authors upon reasonable request.

Code availability

The code used to calculate the results shown in this work is available from the corresponding authors upon reasonable request.

References

48. Zhang, C. et al. Fabrication of silver tips for scanning tunneling microscope induced luminescence. *Rev. Sci. Instrum.* **82**, 083101 (2011).
49. Zhang, L. et al. Electrically driven single-photon emission from an isolated single molecule. *Nat. Commun.* **8**, 580 (2017).
50. Kong, F. F. et al. Probing intramolecular vibronic coupling through vibronic-state imaging. *Nat. Commun.* **12**, 1280 (2021).
51. Le Moal, E., Müller, M., Bauer, O. & Sokolowski, M. Misfit driven azimuthal orientation of NaCl domains on Ag(100). *Surf. Sci.* **603**, 2434–2444 (2009).

Acknowledgements

We thank B. Wang, Y. X. Weng, P. W. Du and Y. Zeng for helpful discussions. This work was supported by the National Key R&D Program of China (Grant No. 2017YFA0303500 and 2016YFA0200600), the National Natural Science Foundation of China (Grant No. 21790352, 21973087, 22174135 and 21622309), the Strategic Priority Research Program of Chinese Academy of Sciences (Grant No. XDB36000000), Anhui Initiative in Quantum Information Technologies (Grant No. AHY090000), Innovation Program for Quantum Science and Technology (Grant No. 2021ZD0303301) and the Fundamental Research Funds for the Central Universities.

Author contributions

Yang Zhang, Z.-C.D. and J.G.H. conceived and designed the experiments. F.-F.K., X.-J.T., S.-H.J., Y.-J.Y. and H.-Y.G. performed experiments and analysed the data. Yao Zhang and G.C. performed theoretical simulations. F.-F.K., Yang Zhang, Yao Zhang, J.-L.Y., Y.L., Z.-C.D. and J.G.H. contributed to the data interpretation. F.-F.K., Yang Zhang, Yao Zhang, Z.-C.D. and J.G.H. co-wrote the manuscript. All authors discussed the results and commented on the manuscript.

Competing interests

The authors declare no competing interests.

Additional information

Extended data is available for this paper at https://doi.org/10.1038/s41565-022-01142-z.

Supplementary information The online version contains supplementary material available at https://doi.org/10.1038/s41565-022-01142-z.

Correspondence and requests for materials should be addressed to Yang Zhang, Zhen-Chao Dong or J. G. Hou.

Peer review information *Nature Nanotechnology* thanks Konstantin E. Dorfman, Yousoo Kim and Takashi Kumagai for their contribution to the peer review of this work.

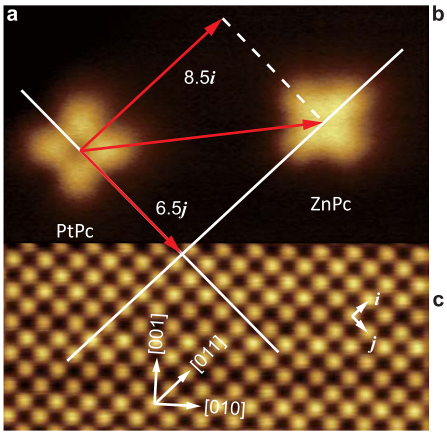

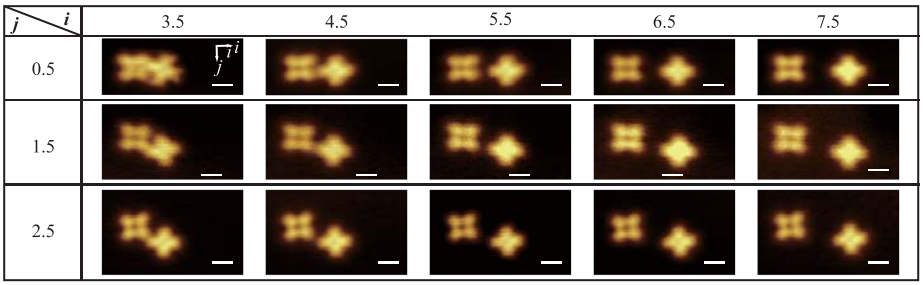

c

i	3.5	3.5	3.5	4.5	4.5	4.5	5.5	5.5	5.5	6.5	6.5	6.5	7.5	7.5	7.5
j	0.5	1.5	2.5	0.5	1.5	2.5	0.5	1.5	2.5	0.5	1.5	2.5	0.5	1.5	2.5
d (nm)	1.41(4)	1.52(4)	1.72(4)	1.81(5)	1.90(5)	2.06(5)	2.21(6)	2.28(6)	2.42(6)	2.61(7)	2.67(7)	2.79(7)	3.01(8)	3.06(8)	3.16(8)

Extended Data Fig. 1 | Estimation on the intermolecular distances for different heterodimer configurations constructed artificially. a, STM image of a single PtPc and a single ZnPc adsorbed on 3ML-NaCl/Ag(100) (7 nm × 7 nm). To identify the molecular adsorption configurations, the STM image was acquired with different scanning conditions: the upper part was acquired at –2.1 V and 2 pA to highlight the molecular skeleton structure, while the lower part was acquired at 0.1 V and 500 pA to resolve the chlorine ions of the NaCl surface. The PtPc center is found to adsorb above a sodium ion with the molecular axes roughly aligned along the [010] or [001] direction, whereas the ZnPc center adsorbs above a chlorine ion with the molecular axes aligned along the [011] or [01$\bar{1}$] direction. The configuration of a PtPc–ZnPc heterodimer is specified with the vector connecting the molecular centers from PtPc to ZnPc. The unit vector ***i*** (***j***) is defined along the [011] ([01$\bar{1}$]) direction between two nearest chlorines. As an example, the PtPc–ZnPc heterodimer in this STM image is noted as (8.5, 6.5) configuration. **b**, STM images of a series of PtPc–ZnPc heterodimers with different configurations. Scale bars, 1 nm. **c**, Estimation of the distances between the PtPc and ZnPc molecules (d), as detailed in Methods. The numbers in parentheses represent the uncertainty of standard deviations. We note that the minimum displacement in molecular manipulation is about 0.40 nm in either ***i*** or ***j*** direction, which is limited by the distance between two nearest chlorines of the NaCl (100) surface.

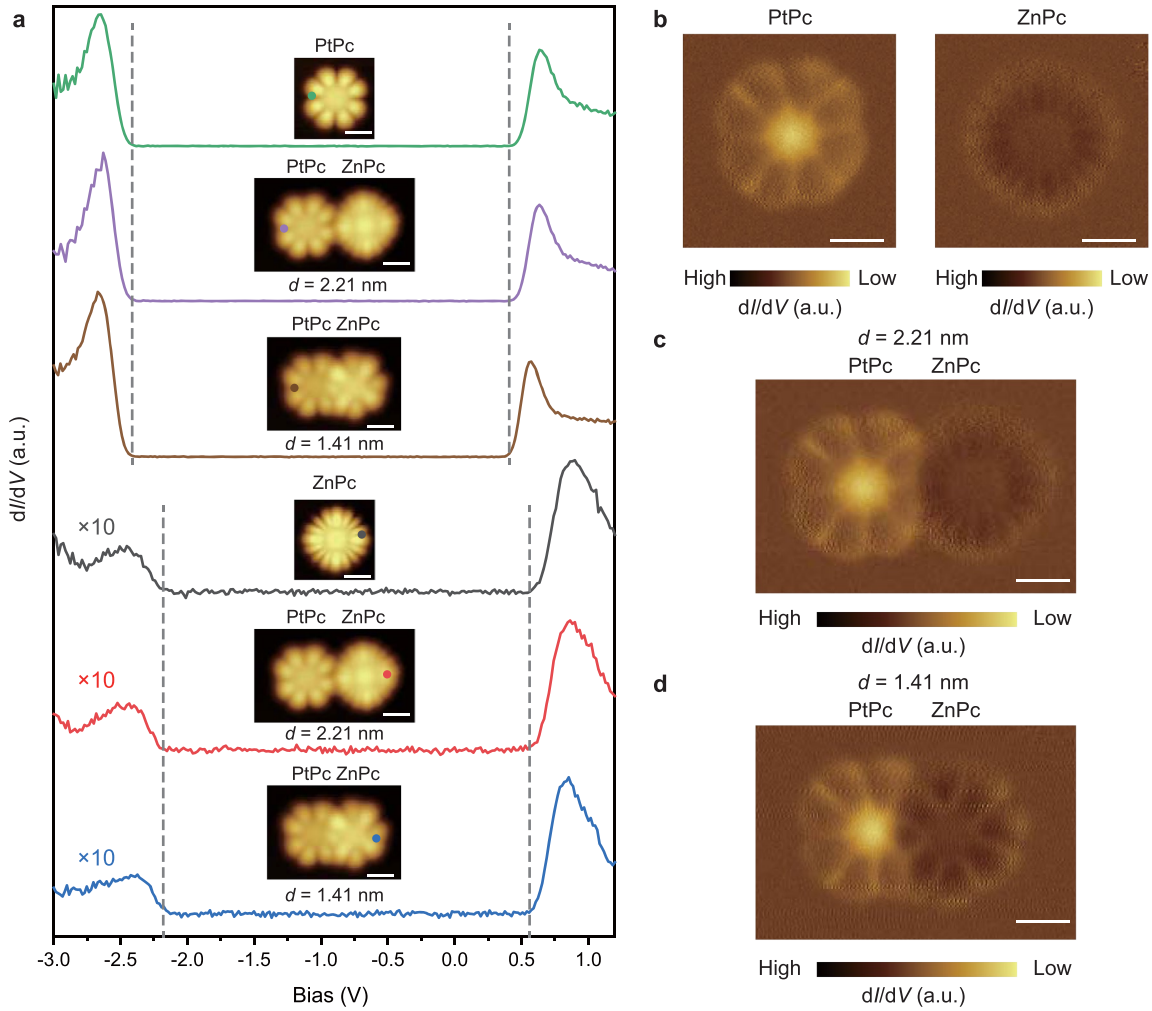

Extended Data Fig. 2 | Comparisons of d*I*/d*V* data for isolated molecules and heterodimers. a, d*I*/d*V* spectra acquired at the lobes of an isolated PtPc (ZnPc) and PtPc–ZnPc dimers for $d = 2.21$ nm and $d = 1.41$ nm, with the measurement position marked by the dots in the inset STM images. The d*I*/d*V* spectra are offset for clarity. The inset shows the corresponding STM images (−2.8 V, 2 pA). **b**, d*I*/d*V* images of an isolated PtPc or ZnPc on the NaCl surface. **c**, d*I*/d*V* image of the PtPc–ZnPc dimer for $d = 2.21$ nm. **d**, d*I*/d*V* image of the PtPc–ZnPc dimer for $d = 1.41$ nm. The d*I*/d*V* signals (images) were measured using the lock-in technique with the tunneling gap set at −2.5 V and 10 pA (−2.8 V and 30 pA). The d*I*/d*V* images were acquired with a closed feedback loop. Scale bars, 1 nm.

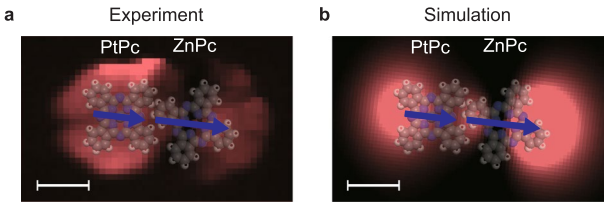

Extended Data Fig. 3 | Spatial distribution of experimental peak intensities and simulated photon image pattern for the P_{dimer} emission of the PtPc–ZnPc heterodimer at $d = 1.41$ nm. a, Spatial distribution of P_{dimer} peak intensities obtained from the STML spectroscopic image (–2.8 V, 30 pA, 1 s per pixel). **b**, Simulated photon image pattern for the P_{dimer} emission. We note that the simulated image in **b** considers the emission process alone, without taking the electron excitation into account. Scale bars, 1 nm. Also detailed in Supplementary Section 11.

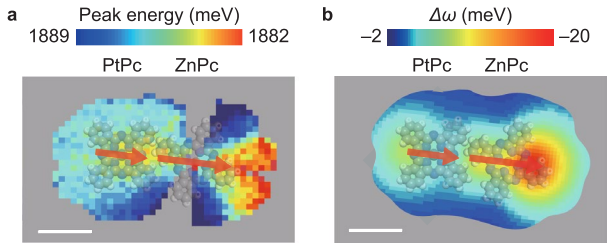

Extended Data Fig. 4 | Spatial distribution of experimental peak energies and simulated photonic Lamb shifts ($\Delta\omega$) for the P_{dimer} emission of the PtPc–ZnPc heterodimer at $d = 1.41$ nm. a, Spatial distribution of P_{dimer} peak energies obtained from the STML spectroscopic image (–2.8 V, 30 pA, 1 s per pixel). **b**, Simulated photonic Lamp shifts ($\Delta\omega$) for the P_{dimer} emission. Note that, in the STML measurements, molecular specific emission peaks can only be identified over the molecular area that can be directly excited by tunneling electrons. Scale bars, 1 nm. Also detailed in Supplementary Section 11.